Two-dimensional MoS$_2$-assisted immediate aggregation of Poly-3-hexylthiophene with high mobility

Yingying Zhang, Shuang Liu, Wenqing Liu, Tao Liang, Xi Yang, Mingsheng Xu*, Hongzheng Chen*

MOE Key Laboratory of Macromolecular Synthesis and Functionalization, State Key Laboratory of Silicon Materials, Department of Polymer Science and Engineering, Zhejiang University, Hangzhou 310027, P. R. China. E-mails: hzchen@zju.edu.cn and msxu@zju.edu.cn

Abstract

Nanoscale morphology is of significance to the electronic properties of semiconducting polymers. Solution-processed poly-3-hexylthiophene (P3HT) has been demonstrated as a promising active-layer material in organic thin film transistors (OTFTs) and solar cells. The controlling of crystallinity of P3HT chains is critical for gaining high-performance devices. Here we demonstrated the immediate crystallization of the P3HT induced by two-dimensional MoS$_2$ nanosheets under ultrasonication. The resultant aggregation was attributed to the presence of interaction between the MoS$_2$ nanosheets and the P3HT, which could enhance inter-chain ordering and association of the P3HT. The crystallization of P3HT contributed to the 38-fold enhancement in the hole mobility of the thin film as compared to the non-crystallized thin films because of the absence of MoS$_2$. Our approach of the using of 2D MoS$_2$ nanosheets to induce immediate aggregation of P3HT provides a facile process to control the crystallization of conjugated polymers for development of high-performance of organic electronics.

Introduction

Solution-processed, semiconducting conjugated polymers have been widely applied in organic optoelectronic devices such as polymer solar cells, organic thin film transistors (OTFTs), and organic phototransistors.[1-4] Poly-3-hexylthiophene (P3HT) is a most promising and studied semiconducting conjugated polymer due to its good solubility in organic solvents and relatively high field-effect mobility.[5-9] The microstructure of regioregular P3HT exhibits a continuous variation in ordering due to the weakly bonded macromolecules with numerous degrees of conformational freedom, which allows to tailor the structure of films with crystalline and amorphous domains.[10] The ordered crystalline domains due to π-π electron coupling can promote polaron delocalization over large length scales for effective charge transport, whereas the amorphous phase limits charge transport.[10] Therefore, it is vital for high-performance transistors to achieve high degree of crystallinity. However, thin films formed from normal solutions often lack good ordering and crystallinity, and thus efforts have been developed to tune their microstructures.[11-17] Thermal annealing is a post-treatment way to improve crystallinity of thin films.[12,13] In contrast to the post-treatment, in-situ crystallization/aggregation in solution[10] or during thin film formation has attracted great interest recently. [11,14,18] Increased crystallinity has been achieved by adding nonsolvent or dopants to a stable P3HT solution,[14-17] spin-coating films under high pressure solvent vapor[18] and exposing the solution to ultrasonic irradiation.[19-23]

Ultrasonic irradiation of solutions is a simple route that could induce a dramatic increase in the degree of crystallinity of the thin film. Zhao *et al.*[21] demonstrated that ultrasonic irradiation helped to decrease chains entanglement during the crystallizing of P3HT in p-xylene and further improved crystalline ordering in spin-coated thin films. Aiyar *et al.*[22] tried to understand ultrasound induced behavior by investigating the influence of solvent, polymer regioregularity (RR) of P3HT and film deposition methods (spin-coating and dip-casting) on the control of crystalline degree, and their

corresponding impact on thin film morphology and charge transport characteristics. They found that the morphology was dependent on both the intrinsic (RR) and extrinsic (film deposition method and solvent) factors. However, following the film deposition, they performed thermal annealing of the deposited films at 110 °C for 10 h, which actually made it difficult to assess the influence of these factors because thermal annealing can affect ordering of the deposited films. Chang et al.[23] found that sequential ultrasonication and UV irradiation of P3HT precursor solution enhanced intra- and inter-molecular ordering, which led to an increase in mobility of the film. However, it is still difficult to fully separate the contributions of the aggregation induced by slow crystallization and the additional process (thermal annealing or UV irradiation) associated with the ultrasonic irradiation. Moreover, achievement of immediate aggregation of P3HT in solution and striking crystallization in the relevant thin film without additional process like thermal annealing is of its advantage in large-area and flexible applications. To our knowledge，little attention has been paid on the immediate aggregation. According to the previous reports,[15,16,24,25] it is reasonable to assume that adding dopants interactive to P3HT chains for ultrasonication may enhance inter-chain ordering/interaction and facilitate immediate aggregation.

As a typical two-dimensional (2D) material, molybdenum disulfide (MoS_2) has been attracting significant attention due to its planar structure and semiconductor characteristics.[26-29] Layered bulk MoS_2 is coupled via weak van der Waals force, which allows to be exfoliated into single layer and few-layer MoS_2.[30] Guan et al.[31] reported a facile method for effective exfoliation of transition metal dichalcogenides in water by using protein, bovine serum albumin (BSA) to produce single layer nanosheets. Benzene rings and disulfides in BSA can strongly bind on the MoS_2 nanosheets via hydrophobic interaction, which results in the exfoliation of MoS_2 bulk into stable monolayer and few-layer MoS_2 nanosheets. Inspired by this, we expect that thiophene group with the similar structure to BSA may interact with MoS_2 nanosheets, and this would induce inter-chain ordering of conjugated polymers.

Here, we report the ordering of P3HT induced by interaction with 2D MoS_2 nanosheets. We present a facile method to produce P3HT-MoS_2 composite solutions through one-step ultrasonication and investigate the influence of MoS_2 on immediate aggregation of P3HT and electric properties of resultant P3HT thin films. Chloroform is used as the solvent because it is difficult for the P3HT in chloroform to form good crystallinity of spin-coated thin films.[14,22] We show that the 2D MoS_2 nanosheets have great influence on the crystallization of P3HT. The field-effect mobility of the resultant P3HT films is improved by ca. 50-fold with 10-time higher of the on/off ratio, as compared to the counterparts without the effect of 2D MoS_2 nanosheets. Our results provide an effective approach to tailor the crystallinity of P3HT by using 2D materials.

Results and Discussion

Figure 1a shows the normalized UV-vis absorption spectra of the supernatant of P3HT-MoS_2, the pristine P3HT and ultrasonicated P3HT solutions. In the range of 500 - 750 nm, the absorption spectra of the pristine P3HT and ultrasonicated P3HT are featureless. By contrast, the UV-vis absorption of P3HT-MoS_2 supernatant shows peaks at 570, 618 and 685 nm. The weak peak at 685 nm is assigned to the A excitonic transition of MoS_2 sheet,[27,32] which also indicates that the MoS_2 nanosheets are semiconducting trigonal prsimatic (2H) phase after the ultrasonication.[33] Figure 1b is the Raman spectra of the corresponding thin films deposited by spin-coating the supernant or solutions onto Si/SiO_2 substrates. Well-defined peaks are observed in the region of 350~1600 cm^{-1}. The main peaks at 1384 and 1452 cm^{-1} are assigned to the in-plane ring skeleton modes of P3HT, *ie.*, symmetric C=C stretch and C-C intraring stretch mode, respectively.[34] The Raman spectrum of P3HT-MoS_2 thin film also has two prominent peaks at 381 and 405 cm^{-1} that correspond to the in-plane E_{2g} and out-of-plane A_{1g} modes of MoS_2, respectively,[35] consistent with the Raman peaks of bulk MoS_2 (see Inset). The absorption and Raman spectra suggest that P3HT-MoS_2 composite is successfully obtained through our one-step ultrasonication.

Despite extensive investigation of ultrasonic-induced aggregation in P3HT solution,[21-23] immediate aggregation cannot be easily achieved. We focus on the effect of 2D MoS$_2$ nanosheets on the immediate aggregation of P3HT under ultrasonication. First, the supernatant of P3HT ultrasonicated with MoS$_2$ (see iii, inset in Figure 1a) is dark purple, which is totally different from that without MoS$_2$ (ii). It is well known that the color change from orange to dark purple is a phenomenon of exhibiting aggregation of P3HT.[20] Second, the UV−vis absorption spectral feature is known to strongly correlate with the structural ordering of π-conjugated polymer,[36,37] which allows to examine aggregation state of the solutions immediately after ultrasonication. The absorption features at 570 nm and 618 nm (Figure 1a) of the P3HT-MoS$_2$ supernatant are indicative of a vibronic structure with a vibronic side band at 570 nm and a 0–0 transition at 610 nm of P3HT, respectively.[36] However, such features are not observed on the pristine and the ultrasonicated P3HT solutions. The observation indicates strong intermolecular π−π interaction and development of crystalline aggregates of P3HT in the P3HT-MoS$_2$ supernatant. This also implies that the MoS$_2$ plays a critical role in aggregation of the P3HT.

The primary effect of ultrasonication on conjugated polymer was reported to increase the interaction between the conjugated polymer and the involved solvent, which slows down the chain entanglement and in turn promotes inter-chain association.[21] However, our ultrasonication of the P3HT without MoS$_2$ resulted in little change of the color and the UV-vis spectrum of the P3HT (Figure 1a). By contrast, when ultrasonicated with MoS$_2$, the UV-vis spectrum indicates aggregation of the P3HT. It is reasonable that the interaction between the P3HT and MoS$_2$ may enhance inter-chain ordering under the sonication. Such an interaction can be inferred by the presence of monolayer MoS$_2$ in the P3HT-MoS$_2$ supernatant (Figure 2), that is, P3HT-assisted MoS$_2$ exfoliation.

Bulk MoS$_2$ can be exfoliated into single layer or few-layer nanosheets by

ultrasonication in appropriate liquid system, which requires a well-matched surface energy of the solvents with MoS_2.[38,39] It has been verified that bulk MoS_2 cannot be successfully exfoliated and monolayer or few-layer MoS_2 cannot be stabilized in chloroform used here, due to the mismatched surface energy of chloroform with MoS_2.[38] However, in our present case, we find that the supernatant of P3HT-MoS_2 remains stable for several weeks without apparent sediment. The transmission electron microscope (TEM) images in Figure 2 show the presence of a quantity of MoS_2 nanoflakes. An interplanar spacing of 0.27 nm measured from the high-resolution TEM (HRTEM) image (Figure 2c) is assigned to the (100) atomic planes of MoS_2.[40] The results suggest that the P3HT acted as an efficient exfoliating agent and there exists interaction between the P3HT and the MoS_2. It has been shown that benzene rings and disulfides groups helped to exfoliate and stabilize MoS_2 nanosheets through binding on the MoS_2 via hydrophobic interaction.[31] It is, thus, supposed that the thiophene group of P3HT, similar to benzene and disulfide groups, may bind on the MoS_2 nanosheets, resulting in successful exfoliation of the bulk MoS_2. This behavior in other terms is that the MoS_2 may enhance inter-chain order or association of P3HT and in turn induces immediate aggregation of P3HT in chloroform. Hence, as depicted in Scheme 1, the exfoliated MoS_2 nanosheets may provide templates for interpolymer ordering of the P3HT under ultrasonication.

The enhanced intermolecular interactions of P3HT chains are expected to lead to high thin-film crystallinity.[41] Atomic force microscopy (AFM) and grazing incidence X-ray diffraction (GIXRD) were employed to investigate the morphological and crystalline properties of the P3HT-MoS_2 thin film. The AFM topographic height and phase images show that the film obtained from the pristine P3HT solution appears featureless and textureless (Figure 3a, 3d). The rapid drying of the spin-coating process due to the volatile chloroform results in a kinetically limited process, which suppresses the formation of ordered structures.[21] Furthermore, no diffraction peak is discernible (Figure 4) of the thin film obtained from the pristine P3HT solution. The thin film obtained from the ultrasonicated P3HT exhibits almost the same feature as

that of the pristine P3HT (Figure 3b, 3e). These results suggest amorphous feature of the thin films. Although the previous report[21,22,42] reported crystalline P3HT thin films when ultrasonic agitation was applied, it is assumed that the molecular weight of P3HT may have close relationship with the self-assembly behaviors under sonication.[21,42] Besides, one should note that the P3HT thin films were annealed at 110 °C for 10 h after the spin-coating of the ultrasonicated solution.[22] In the present study, we did not anneal the spin-coated thin films. As mentioned above, the high vapor rate of chloroform does not allow crystallization of the spin-coated P3HT thin films. By contrast, the topographical image of the thin film obtained from the P3HT-MoS_2 supernatant (Figure 3c) exhibits distinctive characteristics from the pristine and ultrasonicated ones. The corresponding AFM phase image (Figure 3f) clearly shows nanofibrillar networks. The sharp increase in roughness (from 0.609 to 1.999 nm) (Figure 3c) is indicative of the formation of nanofibrillar structures within the thin films.[23] The AFM observation is consistent with the GIXRD spectrum for the thin film obtained from P3HT-MoS_2 supernatant, where an obvious development of (100) peak at 5.16° appears. The (100) diffraction peak is associated with the packing of polymer chain lamellar along the crystallographic direction perpendicular to the backbone.[21,22] The appearance of diffraction peak at 14.36° is corresponding to the (200) peak of MoS_2,[27,29,43] which further confirms the involvement of MoS_2 in the P3HT-MoS_2 supernatant. The results reveal the MoS_2-induced crystallization of P3HT.

The enhanced crystallinity of the P3HT by the 2D MoS_2 nanosheets facilitates carrier transport of the resultant thin film. We fabricated top-contact OTFTs as illustrated in Figure 5a. The active layers of OTFTs were the spin-coated thin films from the pristine P3HT, ultrasonicated P3HT or P3HT-MoS_2 solutions. No further treatment was applied after the spin-coating process. Figure 5b displays the representative transfer characteristics of the devices, and Figure 5c is the output characteristics of the device with the P3HT-MoS_2 as the active layer. A clear transition is observed from the linear to the saturation region until the pinch-off in the accumulation layer. At a

given V_G, I_D first linearly increased and then reached a saturation state with the increase in negative V_{SD}, which suggests a typical *p*-channel OTFTs operation of the P3HT in the accumulation mode. Normally, the field-effect transistor of MoS_2 layer exhibits *n*-type behavior.[44,45] We also measured *n*-channel characteristics of the OTFTs, but did not observe any output or transfer characteristics. This implies that the involved MoS_2 nanosheets did not exhibit field-effect characteristics. Numerical values of the mobility, on/off ratio and threshold voltage are summarized in Table 1. Figure 5d compares the hole mobility of the different OTFTs. The mobilities of the devices of the pristine P3HT and ultrasonicated P3HT are only $9.96 \pm 1.11 \times 10^{-4}$ $cm^2/V \cdot s$ and $1.31 \pm 0.26 \times 10^{-3}$ $cm^2/V \cdot s$, respectively, while that of the P3HT-MoS_2 based device is $5.09 \pm 0.51 \times 10^{-2}$ $cm^2/V \cdot s$, which is about 50-fold of the device with the pristine P3HT and 38-fold of the device with the ultrasonicated P3HT. Similarly, the on/off ratio is also enhanced by one order of magnitude from 10^4 to 10^5. The enhanced OTFT performance of the P3HT with MoS_2 nanosheets can be explained in the view of increased crystallinity of the P3HT.[10] We note that the mobility of the ultrasonicated P3HT is slightly higher than that of the pristine P3HT, indicating ultrasonication has an effect on the electrical properties of the P3HT, though it is hard to discern the morphological and crystalline difference by the AFM and GIXRD characterizations.

To investigate the influence on the electrical properties of the amount of MoS_2 in the P3HT-MoS_2 solution, P3HT-MoS_2 thin films containing different mass of MoS_2 were studied. MoS_2 with initial masses of 1 mg, 5 mg, 10 mg, 15 mg and 20 mg were mixed with the same concentration of P3HT and then ultrasonicated under the same condition. OTFTs based on the resultant P3HT-MoS_2 supernatants were fabricated, the hole mobility and on/off ratio of the transistors are summarized in Table S1. The plot in Figure S1a shows the hole mobility first increased with the initial mass of MoS_2 up to 10 mg, and then a dramatic decrease occurred when the initial mass of MoS_2 was 20 mg. Initial increase (1 mg to 10 mg) in hole mobility can be ascribed by the MoS_2-enhanced crystallinity and ordering of the crystallites. [10,22] The crystalline

properties of P3HT-MoS$_2$ thin films with different amounts of MoS$_2$ (GIXRD, Figure S2) shows that the increased amount of MoS$_2$ in the composites, which is correlated with the initial mass of MoS$_2$ evidenced by the (200) peak of MoS$_2$, led to obvious enhancement in the crystallinity. The scattering mean free path of charge transport in the π-stack is on the order of a nanometer.[46] As a result, the charge transport is mostly affected by such a short-range order of the crystallites and the interconnection of the crystallites.[10] The AFM images (Figure S3) show the clear evolution of P3HT nanofibrillar crystallites in the amorphous matrix of the resulting P3HT-MoS$_2$ thin films. It is observed that the density of the nanofibers in the relevant thin films increased with the increase in initial mass of the MoS$_2$ from 1 mg to 10 mg in P3HT-MoS$_2$ solutions. In the 1 mg MoS$_2$ case, the P3HT nanofibers were limited and sparse. Whereas in the case of 10 mg MoS$_2$, the distance of between the individual P3HT nanofibers was greatly reduced and the nanofibres were connected together, forming efficient carrier transport pathway. However, when the initial mass MoS$_2$ was 20 mg, the on/off ratio and the hole mobility decreased dramatically. The off-state current of the relevant OTFTs is on the order of 10^{-8} A，almost a thousand times higher than those of the other devices, which resulted in a relatively low on/off ratio. Since the overloaded amount of MoS$_2$ from 10 mg to 20 mg contributed little to the enhancement in crystallinity (Figure S2), the dramatic fall in mobility may be mostly due to the introduction of shallow trapping sites by the MoS$_2$. Such a behavior change has been observed in OTFTs consisting of polymer/carbon nanotube and polymer/grapheme composites.[47-49] In addition, percolation type transport mechanism[47], which is associated with the crystalline degree of semiconducting polymers, cannot be ruled out to explain the mobility drop. Although further studies are needed to understand the carrier transport, we find that optimum inclusion of MoS$_2$ is critical for achieving efficient OTFT performance.

Conclusions

We have demonstrated the occurrence of immediate aggregation of the P3HT induced by 2D MoS_2 nanosheets under ultrasonication. Such a crystallization of P3HT was not detected in the process where only ultrasonic irradiation but no MoS_2 was applied, suggesting that the 2D MoS_2 nanosheets play a key role to the crystallization of P3HT. The inter-chain ordering and association of the P3HT may be attributed to the presence of interaction between the 2D MoS_2 nanosheets and the P3HT due to the successful exfoliation of the MoS_2. The aggregates greatly improved the hole transport in the P3HT thin films as manifested by the about 50(38)-fold enhancement of hole mobility of the OTFTs with P3HT-MoS_2 as the active layer, compared to the OTFTs with the pristine P3HT and the P3HT ultrasonicated without MoS_2. Our approach of the using of 2D MoS_2 nanosheets to induce immediate aggregation of P3HT provides a facile process to control the crystallization of conjugated polymers for development of high-performance of organic electronics.

Experimental section

Materials

Regioregular P3HT (Regioregularity > 96%) was purchased from Rieke Metals Inc. (#RM1-001EE) and used without further purification. The molecular weight of P3HT used is 28-34kDa (via GPC) with a dispersion coefficient of 1.7-1.9. Chloroform (anhydrous grade, Sigma Aldrich) was used as purchased. Pristine MoS_2 (particle size > 1.8 μm，Aldrich) was used as purchased.

Solution preparation and device fabrication

Solutions of P3HT were prepared at a concentration of 4 mg/ml by heating the

solution on a hot plate at a temperature close to 55 °C, the boiling point of chloroform as the solvent.[21] Bulk MoS_2 with different mass (0, 1, 5, 10 or 20 mg) was directly mixed with 2 ml resolved P3HT/ chloroform solution and then the mixture went through ultrasonic irradiation for 20 min. An ultrasonic cleaner (KQ3200E, 40 KHz, 150 W) was used for ultrasonic irradiation. The solutions were prepared and ultrasonicated in sealed glass vials to prevent solvent evaporation. After ultrasonication and stewing, supernatants were collected for further characterizations and OTFTs fabrication. Solutions of pristine P3HT and ultrasonicated P3HT without MoS_2 with the same concentration as the supernatant were used as controls.

The thin films for OTFTs were prepared via spin-coating the collected supernatants at a speed of 1500 rpm for 40 s onto highly doped silicon substrates with 300 nm SiO_2. Prior to the deposition of the blended solution, the substrates were modified by divinyltetramethyldisiloxane bis(benzocyclobutene) (BCB, Dow Chemicals) thin layers that were spin-coated from a mesitylene (Acros) solution(V_{BCB} : $V_{mesitylene}$ = 1 : 30) and thermally cross-linked on a hot plate in a N_2 glove box at the temperature of 120 °C (30 min), 180 °C (30 min) and 240 °C (30 min). The top-contact source and drain electrodes were 100 nm Au. The channel length (L) and channel width (W) of the OTFTs were 50 μm and 1 mm, respectively. Control devices with pristine P3HT and ultraonicated P3HT as the active layer were also fabricated. Both the thin film preparation and device fabrication were conducted in a nitrogen-filled glove box with less than 1 ppm of oxygen and moisture.

Electrical characterization of the devices

Electrical characterization of the devices was performed using a Keithley 4200-SCS semiconductor parameter analyser (Keithley) in a N_2 atmosphere inside a glove box. The field-effect mobility (μ) of OTFTs was extracted from the transfer characteristics using a linear fit to the plot of the square root of saturation source–drain current (I_D) as a function of the gate voltage V_G, as shown in the following equation.

$$I_D = \frac{W}{L} C \mu (V_G - V_{TH})^2,$$

Where V_{TH} is threshold voltage, $C (= 10 \text{ nF cm}^{-2})$ is the measured capacitance of the BCB-covered SiO_2/Si substrates.[50] For statistics, data of hole mobility from fifteen devices are presented as mean ± SD.

Instrumentation

The UV-vis spectra of the collected supernatants or solutions were recorded on a UV-Visible spectrophotometer (UV-2450, Shimadzu Corporation, Japan). Atomic force microscopy (AFM) images were obtained using a Veeco Multimode atomic force microscopy in the tapping mode. Raman spectra were performed on inVia Raman microscope. The Grazing Incidence X-ray Diffraction (GIXD) patterns were recorded at a scan rate of 5°/min on the Rigaku D/max-2550PC X-ray diffractometer with Cu Kα radiation (λ=1.5406 nm) operating at 45 kV and 40 mA. Grazing incidence angle was scanned from 3° to 20°. Samples for GIXD measurements were prepared by spin-coating the supernatants or solutions onto hydrophilic silicon substrates having a native oxide, which were cleaned in an ultrasonic bath of acetone and isopropanol. All samples used for the AFM, Raman and GIXD characterizations were prepared by the same process as those for OTFTs fabrication with the identical supernatants or solutions. Transmission electron microscope (TEM) images were taken by a FEI TECNAI G2 F20-TWIN TEM. Samples for TEM measurement were prepared by pipetting a few milliliters of the diluted supernatant onto holey carbon mesh grids

(230 mesh).

References

1   H. Sirringhaus, N. Tessler and R. H. Friend, *Science*, 1998, **280**, 1741–1744.

2   A. Facchetti, *Chem. Mater.*, 2011, **23**, 733–758.

3   Y.-H. Chou, H.-C. Chang, C.-L. Liu and W.-C. Chen, *Polym. Chem.*, 2014, **6**, 341–352.

4   H. A. Um, D. H. Lee, D. U. Heo, D. S. Yang, J. Shin, H. Baik, M. J. Cho and D. H. Choi, *ACS Nano*, 2015, **9**, 5264–5274.

5   H. Sirringhaus, P. J. Brown, R. H. Friend, M. M. Nielsen, K. Bechgaard, B. M. W. Langeveld-Voss, A. J. H. Spiering, R. a. J. Janssen, E. W. Meijer, P. Herwig and D. M. de Leeuw, *Nature*, 1999, **401**, 685–688.

6   B. W. Boudouris, V. Ho, L. H. Jimison, M. F. Toney, A. Salleo and R. A. Segalman, *Macromolecules*, 2011, **44**, 6653–6658.

7   L. Zhang, W. Zhou, J. Shi, T. Hu, X. Hu, Y. Zhang and Y. Chen, *J. Mater. Chem. C*, 2015, **3**, 809–819.

8   H. G. O. Sandberg, G. L. Frey, M. N. Shkunov, H. Sirringhaus, R. H. Friend, M. M. Nielsen and C. Kumpf, *Langmuir*, 2002, **18**, 10176–10182.

9   Z. Bao, A. Dodabalapur and A. J. Lovinger, *Appl. Phys. Lett.*, 1996, **69**, 4108–4110.

10 R. Noriega, J. Rivnay, K. Vandewal, F. P. V. Koch, N. Stingelin, P. Smith, M. F. Toney and A. Salleo, *Nat. Mater.*, 2013, **12**, 1038–1044.

11 M. Xu, K. Nagai, M. Nakamura, K. Kudo and M. Iizuka, *Appl. Phys. Lett.*, 2007, **90**, 223512-223512.

12 K. Kanai, T. Miyazaki, H. Suzuki, M. Inaba, Y. Ouchi and K. Seki, *Phys. Chem. Chem. Phys.*, 2009, **12**, 273–282.

13 E. Verploegen, C. E. Miller, K. Schmidt, Z. Bao and M. F. Toney, *Chem. Mater.*, 2012, **24**, 3923–3931.

14 J.-F. Chang, B. Sun, D. W. Breiby, M. M. Nielsen, T. I. Sölling, M. Giles, I. McCulloch and H. Sirringhaus, *Chem. Mater.*, 2004, **16**, 4772–4776.

15 Y. D. Park, H. S. Lee, Y. J. Choi, D. Kwak, J. H. Cho, S. Lee and K. Cho, *Adv. Funct. Mater.*, 2009, **19**, 1200–1206.

16 Y. Guo, Y. Han and Z. Su, *J. Phys. Chem. B*, 2013, **117**, 14842–14848.

17 W. Zhou, J. Shi, L. Lv, L. Chen and Y. Chen, *Phys. Chem. Chem. Phys.*, 2014, **17**, 387–397.

18 D. H. Kim, Y. Jang, Y. D. Park and K. Cho, *J. Phys. Chem. B,* 2006, **110**, 15763–15768.

19 A. R. Aiyar, J.-I. Hong, R. Nambiar, D. M. Collard and E. Reichmanis, *Adv. Funct. Mater.*, 2011, **21**, 2652–2659.

20 B.-G. Kim, M.-S. Kim and J. Kim, *ACS Nano*, 2010, **4**, 2160–2166.

21 K. Zhao, L. Xue, J. Liu, X. Gao, S. Wu, Y. Han and Y. Geng, *Langmuir*, 2010, **26**, 471–477.

22 A. R. Aiyar, J.-I. Hong, J. Izumi, D. Choi, N. Kleinhenz and E. Reichmanis, *ACS Appl. Mater. Interfaces*, 2013, **5**, 2368–2377.

23 M. Chang, J. Lee, P.-H. Chu, D. Choi, B. Park and E. Reichmanis, *ACS Appl. Mater. Interfaces*, 2014, **6**, 21541–21549.

24 S. Nam, J. Kim, H. Lee, H. Kim, C.-S. Ha and Y. Kim, *ACS Appl. Mater. Interfaces*, 2012, **4**, 1281–1288.

25 X. Yu, K. Xiao, J. Chen, N. V. Lavrik, K. Hong, B. G. Sumpter and D. B. Geohegan, *ACS Nano*, 2011, **5**, 3559–3567.

26   M. Xu, T. Liang, M. Shi and H. Chen, *Chem. Rev.*, 2013, **113**, 3766–3798.

27   W. Liu, X. Yang, Y. Zhang, M. Xu and H. Chen, *RSC Adv.*, 2014, **4**, 32744–32748.

28   X. Yang, W. Fu, W. Liu, J. Hong, Y. Cai, C. Jin, M. Xu, H. Wang, D. Yang and H. Chen, *J. Mater. Chem. A*, 2014, **2**, 7727–7733.

29   X. Yang, W. Liu, M. Xiong, Y. Zhang, T. Liang, J. Yang, M. Xu, J. Ye and H. Chen, *J. Mater. Chem. A*, 2014, **2**, 14798–14806.

30   V. Nicolosi, M. Chhowalla, M. G. Kanatzidis, M. S. Strano and J. N. Coleman, *Science*, 2013, **340**, 1226419-1226419.

31   G. Guan, S. Zhang, S. Liu, Y. Cai, M. Low, C. P. Teng, I. Y. Phang, Y. Cheng, K. L. Duei, B. M. Srinivasan, Y. Zheng, Y.-W. Zhang and M.-Y. Han, *J. Am. Chem. Soc.*, 2015, **137**, 6152–6155.

32   L. Muscuso, S. Cravanzola, F. Cesano, D. Scarano and A. Zecchina, *J. Phys. Chem. C*, 2015, **119**, 3791–3801.

33   R. Lv, J. A. Robinson, R. E. Schaak, D. Sun, Y. Sun, T. E. Mallouk and M. Terrones, *Acc. Chem. Res.*, 2014,**48**,56-64

34   W. C. Tsoi, D. T. James, J. S. Kim, P. G. Nicholson, C. E. Murphy, D. D. C. Bradley, J. Nelson and J.-S. Kim, *J. Am. Chem. Soc.*, 2011, **133**, 9834–9843.

35   C. Lee, H. Yan, L. E. Brus, T. F. Heinz, J. Hone and S. Ryu, *ACS Nano*, 2010, **4**, 2695–2700.

36   S. D. D. V. Rughooputh, S. Hotta, A. J. Heeger and F. Wudl, *J. Polym. Sci. Part B Polym. Phys.*, 1987, **25**, 1071–1078.

37   J. Clark, C. Silva, R. H. Friend and F. C. Spano, *Phys. Rev. Lett.*, 2007, **98**, 206406.

38   J. N. Coleman, M. Lotya, A. O'Neill, S. D. Bergin, P. J. King, U. Khan, K. Young, A. Gaucher, S. De, R. J. Smith, I. V. Shvets, S. K. Arora, G. Stanton, H.-Y. Kim, K. Lee, G. T. Kim, G. S. Duesberg, T. Hallam, J. J. Boland, J. J. Wang, J. F. Donegan, J. C. Grunlan, G. Moriarty, A. Shmeliov, R. J. Nicholls, J. M. Perkins, E. M. Grieveson, K. Theuwissen, D. W. McComb, P. D. Nellist and V. Nicolosi, *Science*, 2011, **331**, 568–571.

39 G. Cunningham, M. Lotya, C. S. Cucinotta, S. Sanvito, S. D. Bergin, R. Menzel, M. S. P. Shaffer and J. N. Coleman, *ACS Nano*, 2012, **6**, 3468–3480.

40 X. Wang, X. Shen, Z. Wang, R. Yu and L. Chen, *ACS Nano*, 2014, **8**, 11394–11400.

41 M. Chang, D. Choi, B. Fu and E. Reichmanis, *ACS Nano*, 2013, **7**, 5402–5413.

42 K. Zhao, H. U. Khan, R. Li, Y. Su and A. Amassian, *Adv. Funct. Mater.*, 2013, **23**, 6024–6035.

43 K. F. Mak, C. Lee, J. Hone, J. Shan and T. F. Heinz, *Phys. Rev. Lett.*, 2010, **105**, 136805-136805.

44 B. Radisavljevic, A. Radenovic, J. Brivio, V. Giacometti and A. Kis, *Nat. Nanotechnol.*, 2011, **6**, 147–150.

45 B. Radisavljevic and A. Kis, *Nat. Mater.*, 2013, **12**, 815–820.

46 R. A. Street, J. E. Northrup and A. Salleo, *Phys. Rev. B*, 2005, **71**, 165202.

47 J. N. Coleman, S. Curran, A. B. Dalton, A. P. Davey, B. McCarthy, W. Blau and R. C. Barklie, *Phys. Rev. B*, 1998, **58**, R7492–R7495.

48 M. E. Gemayel, A. Narita, L. F. Dössel, R. S. Sundaram, A. Kiersnowski, W. Pisula, M. R. Hansen, A. C. Ferrari, E. Orgiu, X. Feng, K. Müllen and P. Samorì, *Nanoscale*, 2014, **6**, 6301–6314.

49 C.-J. Lin, C.-L. Liu and W.-C. Chen, *J. Mater. Chem. C*, 2015, **3**, 4290–4296.

50 C. Fan, A. P. Zoombelt, H. Jiang, W. Fu, J. Wu, W. Yuan, Y. Wang, H. Li, H. Chen and Z. Bao, *Adv. Mater.*, 2013, **25**, 5762–5766.

Figures
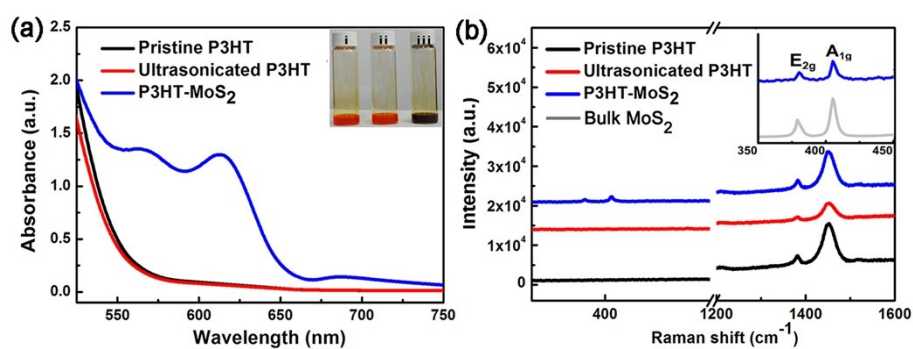
Figure 1. (a) UV−vis absorption spectra of (i) pristine P3HT solution, (ii) ultrasonicated P3HT solution, and (iii) P3HT-MoS$_2$ supernatant. The inset photos were taken immediately after employing ultrasonication for 20 min and presented the aggregation behaviors of P3HT containing MoS$_2$ under ultrasonication; (b) Raman spectra for thin films spin-coated from pristine P3HT and P3HT-MoS$_2$ solutions onto the Si/SiO$_2$ substrates. The insert of (b) shows the detailed Raman spectra of the bulk MoS$_2$ and P3HT-MoS$_2$ ranged from 350 to 450 nm. The mass of MoS$_2$ involved in the initial P3HT-MoS$_2$ solution is 10 mg.
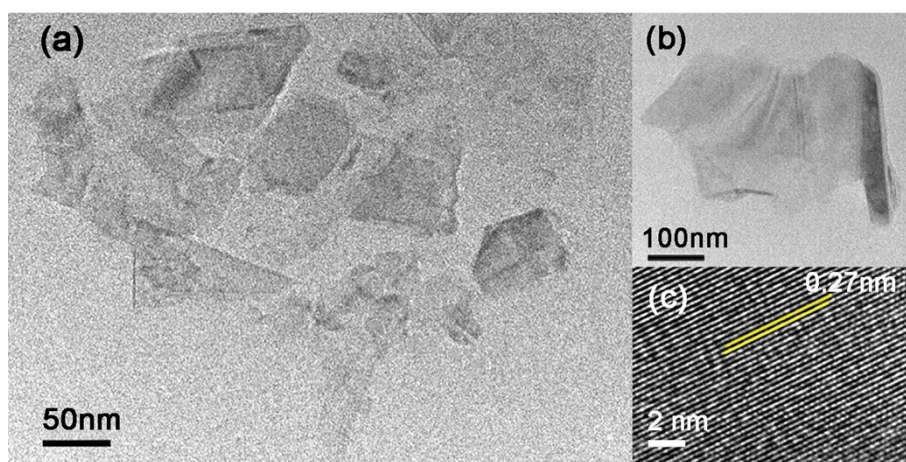
Figure 2. (a) Low-resolution TEM image of MoS_2 flakes obtained by ultrasonication of P3HT-MoS_2 in chloroform solution; (b) A selected MoS_2 ultrathin nanosheet with the average size of 200 nm, (c) High-resolution TEM images of the related MoS_2 nanosheet.
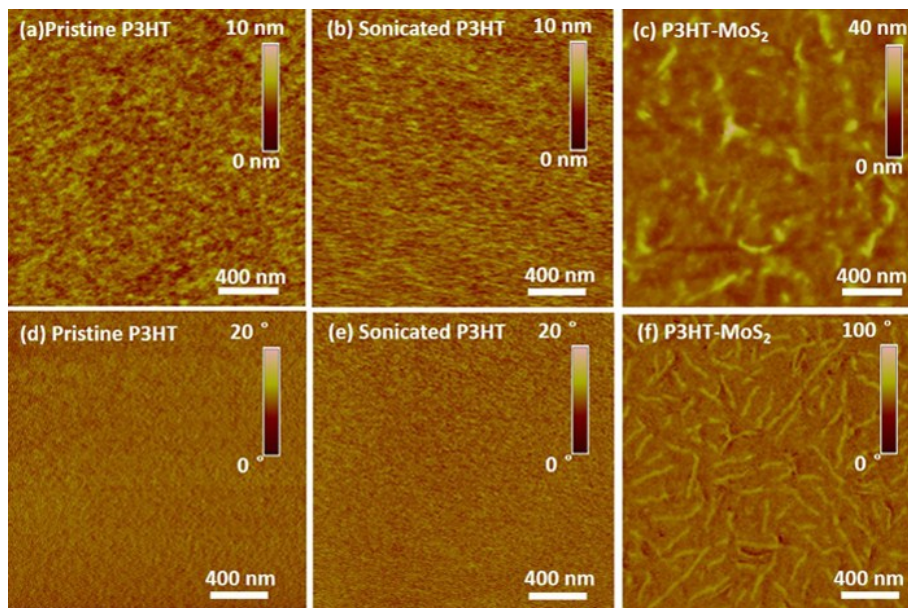
Figure 3. AFM images (scan size: 2 μm × 2 μm; (a-c) height mode, (d-f) phase mode) of P3HT-MoS$_2$ thin films obtained from different solutions. (a, d) Pristine P3HT, (b, e) Sonicated P3HT, (c, f) P3HT-MoS$_2$. The thin films were spin-coated from solutions or supernatant onto BCP/SiO$_2$/Si substrates by the same process as for OTFTs fabrication. RMS roughness of the thin film in (a), (b) and (c) is 0.609, 0.585 and 1.999 nm, respectively. The mass of MoS$_2$ involved in the initial P3HT-MoS$_2$ solution is 10 mg.
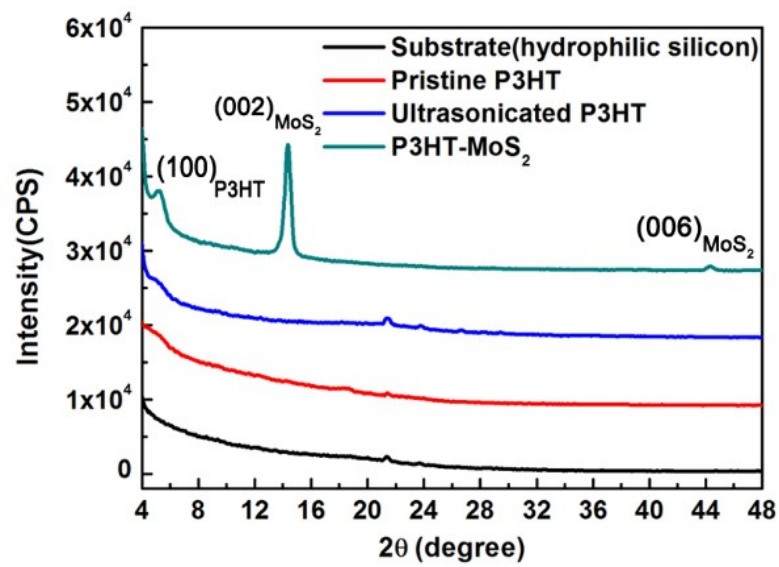
Figure 4. GIXRD profiles of thin films obtained by spin-coating the three different solutions (i and ii in Figure 1a) or supernatant (iii) onto hydrophilic silicon substrates with native oxide.
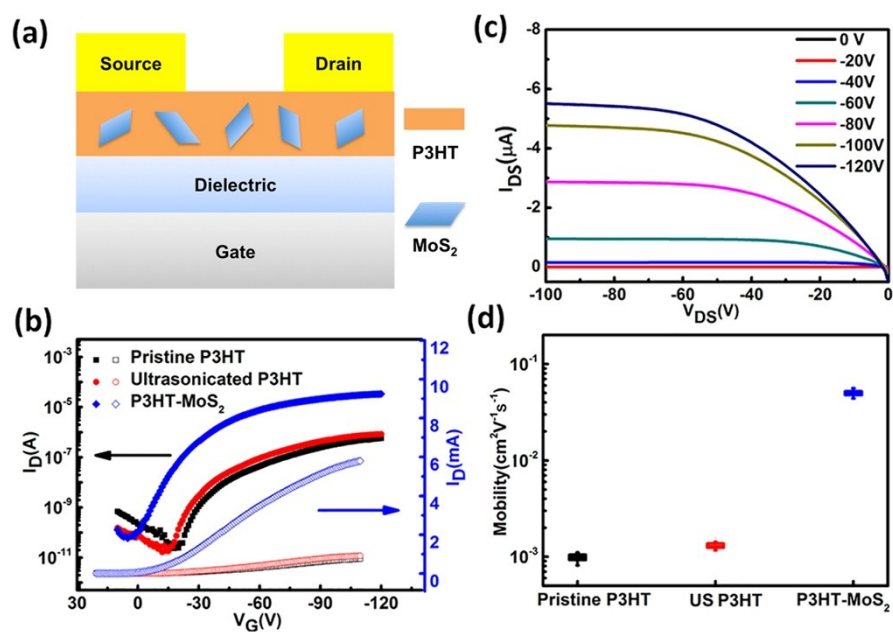
Figure 5. (a) Scheme of the OTFT devices; (b) Representative transfer characteristics of OTFTs based on the pristine P3HT, ultrasonicated P3HT (US P3HT) and P3HT-MoS$_2$; (c) Output characteristics of P3HT-MoS$_2$ OTFT; (d) Hole mobility of the different OTFTs.

Scheme 1. Schematic illustration of P3HT aggregation under ultrasonication containing 2D MoS$_2$ nanosheets.

Table 1. Electrical properties of three different OTFTs.

OTFTs	Mobility (cm^2/V·s)	On/Off ratio (-)
Pristine P3HT	$9.96\pm1.11\times10^{-4}$	$4.81\pm2.55\times10^{4}$
Ultrasonicated P3HT	$1.31\pm0.26\times10^{-3}$	$5.37\pm2.00\times10^{4}$
P3HT-MoS_2	$5.09\pm0.51\times10^{-2}$	$5.81\pm2.07\times10^{5}$